

Time-lapse seismic data inversion for estimating reservoir parameters using deep learning

Harpreet Kaur¹, Zhi Zhong², Alexander Sun¹, and Sergey Fomel¹

Abstract

Geologic carbon sequestration involves the injection of captured carbon dioxide (CO₂) into subsurface formations for long-term storage. The movement and fate of the injected CO₂ plume is of great concern to regulators because monitoring helps to identify potential leakage zones and determines the possibility of safe long-term storage. To address this concern, we design a deep-learning framework for CO₂ saturation monitoring to determine the geologic controls on the storage of the injected CO₂. We use different combinations of porosities and permeabilities for a given reservoir to generate saturation and velocity models. We train the deep-learning model with a few time-lapse seismic images and their corresponding changes in saturation values for a particular CO₂ injection site. The deep-learning model learns the mapping from the change in the time-lapse seismic response to the change in CO₂ saturation during the training phase. We then apply the trained model to data sets comprising different time-lapse seismic image slices (corresponding to different time instances) generated using different porosity and permeability distributions that are not part of the training to estimate the CO₂ saturation values along with the plume extent. Our algorithm provides a deep-learning assisted framework for the direct estimation of CO₂ saturation values and plume migration in heterogeneous formations using the time-lapse seismic data. Our method improves the efficiency of time-lapse inversion by streamlining the large number of intermediate steps in the conventional time-lapse inversion workflow. This method also helps to incorporate the geologic uncertainty for a given reservoir by accounting for the statistical distribution of porosity and permeability during the training phase. Tests on different examples verify the effectiveness of our approach.

Introduction

With rising concerns around global warming, carbon capture and the geologic storage (CCS) of carbon dioxide (CO₂) has become a promising way to reduce anthropogenic CO₂ emission in the atmosphere (Ivanova et al., 2012). Several sites have been assigned for underground sequestration of CO₂ at a variety of scales (Vasco et al., 2019), ranging from smaller volumes for research purposes, such as at Ketzin, Germany (Ivanova et al., 2012), and Otway, Australia (Pevzner et al., 2017) to large-scale commercial operations, such as Sleipner, Norway (Chadwick et al., 2014; Eiken, 2019), and In Salah, Algeria (Ringrose et al., 2013; Vasco et al., 2018). Currently, carbon sequestration with enhanced oil recovery (EOR) is a promising technology for emission management because it increases the recovery of existing oil reserves and bridges the gap between regional-scale CO₂ capture and geologic sequestration

(Dai et al., 2014; Zhong et al., 2019a). CO₂ sequestration with EOR is an important development for climate change policy because almost all of the injected CO₂ remains underground after the fields are decommissioned.

However, because subsurface formations are heterogeneous and also contain many fractures and faults, a significant risk exists of CO₂ leakage into the overlying rock. In addition, CO₂ also can interact chemically with the rock in which it is stored, complicating the prediction of the transport behavior of the CO₂. Leakage of CO₂ can lead to the acidification of the groundwater, killing of plant life, and surface/subsurface mineral right infringement and asset damage (Sun et al., 2013). Because the aim of the CCS project is to achieve the effective storage of the injected CO₂, while mitigating the potential leakage risks, the development of robust and accurate workflows is necessary for tracking CO₂ plume migration in the subsurface.

¹The University of Texas at Austin, Bureau of Economic Geology, John A. and Katherine G. Jackson School of Geosciences, University Station, Box X, Austin, Texas 78713-8924, USA. E-mail: harpreet@utexas.edu (corresponding author); alex.sun@beg.utexas.edu; sergey.fomel@beg.utexas.edu.

²China University of Geosciences, Wuhan 430074, China. E-mail: zhongzhi@cug.edu.cn.

Manuscript received by the Editor 9 October 2020; revised manuscript received 26 September 2021; published ahead of production 1 December 2021; published online 12 January 2022. This paper appears in *Interpretation*, Vol. 10, No. 1 (February 2022); p. T167–T179, 12 FIGS., 2 TABLES. <http://dx.doi.org/10.1190/INT-2020-0205.1>. © 2022 Society of Exploration Geophysicists and American Association of Petroleum Geologists

Monitoring the movement of the injected CO₂ and its impact on subsurface properties contributes to our understanding of its fate upon leaving the well (Vasco et al., 2019). Imaging and monitoring CO₂ movement is important to make sure that the CO₂ is injected at the correct depth and location; it does not migrate toward high-leakage risk areas like major faults with a weak seal; and it does not interfere with subsurface operations such as oil, groundwater, gas, or minerals (Lumley, 2010). Four-dimensional seismic methods, which involve repeating 3D seismic surveys in a time-lapse mode, are viewed as one of the most important methods for providing a relatively effective means of monitoring the changes in the subsurface due to the injection and storage of CO₂ for sequestration projects (Kazemeini et al., 2010; Lumley, 2010). The variable properties of CO₂ with reservoir pressure and temperature and the variable properties of reservoir rocks saturated with CO₂-fluid mixtures after injection determine the strength of the signal (Lumley, 2010).

Surface seismic data cover wider areas and have a more important role in the large-scale monitoring of CO₂ than borehole seismic data, which are only available near existing wells. However, the applicability of the seismic monitoring method depends on the effect of the injected carbon dioxide on the elastic properties of the media along with the resultant change in the propagation of the seismic waves through the media. Surface seismic monitoring, such as time-lapse seismic monitoring, has proven useful in imaging the propagation of CO₂ and identifying potential CO₂ leakages at different sites, including the In Salah storage project (Gibson-Poole and Raikes, 2010; Zhang et al., 2015), the Weyburn EOR project (White, 2011), and the Aquis-tore field site (White et al., 2015). However, the nonlinear and ill-posed nature of the problem makes extraction of parameter from the seismic data a complicated inverse problem. An ambiguity results from the possibility that several different combinations of shear and acoustic impedances can generate equivalent rock properties. The nonuniqueness is exacerbated because the errors from inversion are forward propagated into the predictions of static (porosity and net to gross) and dynamic (pressure, saturation, and temperature change) properties from the seismic-derived attributes.

Previous studies proposed several methods for estimating the dynamic reservoir properties using the time-lapse seismic data. These methods fall into two categories: the stochastic method and the deterministic methods. Johansen et al. (2004) design an inversion framework for estimating rock-physics properties from seismic data by using specific rock-physics constraints. Eidsvik et al. (2004), Tarantola (2005), Bachrach (2006), and Grana and Della Rossa (2010) use Bayesian inversion, which is a stochastic approach, for lithology and reservoir characterization. Tian and MacBeth (2015) design a 4D seismic inversion workflow using a coupled Bayesian scheme that combines static and dynamic loop methods to avoid rescaling issues and to reduce the

nonuniqueness of 4D seismic inversion. Assunção et al. (2016) propose a stochastic inversion scheme to obtain pressure change and water saturation maps from 4D seismic data. Grana and Mukerji (2015) propose the Bayesian inversion of time-lapse seismic data for estimating the changes in the static and dynamic properties of the reservoir. Landrø (2001), Landrø et al. (2003), and Dadashpour et al. (2008) use direct inversion methods based on the approximations of the analytical expression of pressure and saturation changes as a function of the reflectivity coefficient where the approximated saturation and pressure values are comparable with the dynamic reservoir model predictions (Grana and Mukerji, 2015). Buland and El Ouair (2006) and Trani et al. (2011) propose a probabilistic approach for time-lapse seismic inversion. Maleki et al. (2018) combine the time-lapse seismic data, reservoir simulation model, and production data to identify the reservoir flow pattern.

The estimation of the rock-physics model from the seismic data is a highly underdetermined problem. The number of model parameters often is higher than the number of available data parameters, which hinders our ability to perform an accurate inversion of the rock-physics model. Furthermore, P-wave velocity varies nonlinearly with saturation, making this inverse problem highly nonlinear. Conventionally, these types of problems are solved by either reducing the number of subsurface model parameters or by using a priori information as regularization constraints (Sun and Sun, 2015). However, these approximations can reduce the accuracy of inversion results. In addition, seismic data are noisy, and its vertical resolution is lower than the dynamic property change. Therefore, it is important to take into consideration the uncertainties in pressure and saturation changes (Johansen et al., 2013).

Recently, neural networks have shown promising results in solving inverse problems. Zheng and Zhang (2018) propose a neural network-based approach for prestack seismic inversion. Richardson (2018) performs full-waveform inversion using neural networks. Fu et al. (2019) implement a neural network-based forward model for seismic waveform inversion. Wang et al. (2020) propose a closed loop convolutional neural network for seismic inversion. In this paper, we propose the use of deep neural networks (DNNs) for performing the nonlinear mapping from time-lapse seismic data to CO₂ saturation. The proposed method incorporates uncertainty information by accounting for the statistical distribution of porosity and permeability and circumvents iterative inversion for the saturation estimation from seismic data. The proposed workflow also improves the efficiency of the conventional inversion algorithms by circumventing the need for intermediary steps. We test the proposed method using a synthetic model and compare the results with the saturation calculation using numerical simulations. The proposed method can easily be extended to jointly invert for multiple reservoir properties.

Methodology

- 1) We generate the stochastic realizations of the permeability distribution. The stochastic permeability field for one of the instances along with the histogram of the permeability distribution is shown in Figure 1. The porosity distribution is assumed to be linearly connected with log permeability. The equation relating permeability and porosity is obtained by fitting the log data where intercept and slope are fitting coefficients. The porosity distribution is computed from the simulated permeability distribution using the following relationship (Zhong et al., 2019b):

$$\phi = 0.05(\ln(k) + 2) + 0.05, \quad (1)$$

where k and ϕ denote the permeability and porosity, respectively. In practice, most countries now require a detailed storage site characterization before commencement of injection. The baseline site characterization data (e.g., well logs and seismic data) may be used to construct a geologic model and to parameterize the fluid flow model.

- 2) We generate the fluid model by assuming that the fluid flow system consists of two components, brine and CO_2 , with two phases, liquid and gas. The fluid flux is governed by Darcy's law for multiphase flows:

$$q_\alpha = \frac{-k_{r,\alpha}k(\nabla P_\alpha - \rho_\alpha g \nabla z)}{\mu_\alpha}, \quad (2)$$

where the subscript α denotes either the liquid or the gas phase, q_α is the phase flux, k is the absolute permeability, $k_{r,\alpha}$ is the relative permeability, ρ_α and μ_α are the density and viscosity of each phase α , respectively, P_α is the fluid pressure of phase α , g is the gravitational constant, and z is the reservoir depth. The corresponding mass conservation equations are given by the following coupled partial differential equations:

$$\frac{\partial(\phi S_\alpha)}{\partial t} = \nabla \cdot q_\alpha + q_{f,\alpha}, \quad (3)$$

where ϕ is the porosity, S_α is the water ($\alpha = w$) and gas ($\alpha = g$) saturations with the constraint $S_w + S_g = 1$, and $q_{f,\alpha}$ is the sink/source terms. Simulated water saturation (S_w) and gas saturation (S_g) maps are obtained by solving equation 3 using different porosity and permeability distributions (which we shall refer to as realizations) and are saved at monthly intervals. For this study, we used a commercial compositional reservoir simulator (CMG GEM) that discretizes equation 3 into finite-difference

forms using the first-order backward differences in time and central differences in space. In addition, the fluid pressures of the fluid system are related through capillary pressure $P_{c,w}$ as

$$P_g = P_w + P_{c,w}. \quad (4)$$

- 3) Then, we build the rock-physics model, which relates the elastic rock properties, such as velocity and impedance, and the reservoir properties, such as fluid saturation and porosity. To compute the bulk density (ρ_b), which consists of two parts, the solid rock density (ρ_m) and the effective fluid density (ρ_{fe}), we use the following equation:

$$\rho_b = \phi \sum_{\alpha=w,g} S_\alpha \rho_{f,\alpha} + (1 - \phi) \sum_{j=1}^N f_{m(j)} \rho_{m(j)}, \quad (5)$$

where $\sum S_\alpha \rho_{f,\alpha}$ represents the effective density of the multifluid mixture (ρ_{fe}), $\rho_{f,\alpha}$ and S_α are the density and saturation, respectively, of the individual fluid $\alpha = w$ for water and $\alpha = g$ for gas, $f_{m(j)}$ is the volume fraction of the mineral constituent j , $\rho_{m(j)}$ is the density of mineral constituent j , N is the total number of minerals in the rock, and $\rho_{f,\alpha}$ is the fluid density, which is a function of pressure, temperature, and salinity. We used the Batzle-Wang model (Batzle and Wang, 1992) to calculate the gas and brine density at different pressures. The values of density, elastic properties, and fractions of each rock mineral used in this study are listed in Table 1. For the given reservoir parameters, such as porosity, mineral content, and water saturation, the modulus and elastic properties (such as acoustic impedance) of the solid phase, dry rock, and fluid phase may be calculated using the Voigt-Reuss-Hill model (Mavko et al., 1998), Wood's equation (Mavko et al., 1998), and the Hertz-Mindlin model (Dadashpour et al., 2008). The elastic modulus of the solid phase ($K_{\text{matrix}}, G_{\text{matrix}}$) is obtained using the Voigt-Reuss-Hill average of the mineral constituents

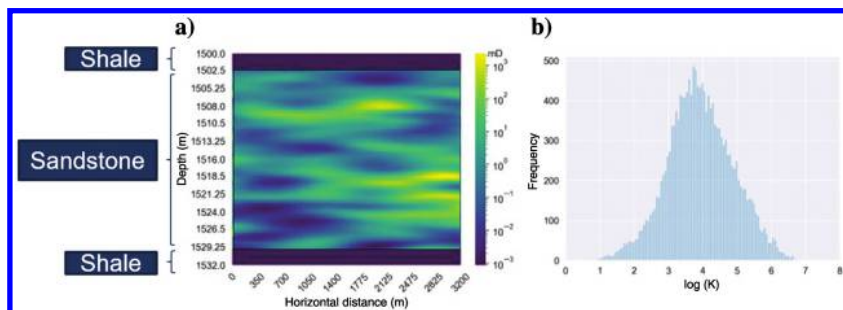


Figure 1. (a) Stochastic permeability field generated using the SGSIM for the base case, where the top and the bottom layers correspond to the shale sections that serve as reservoir seals and the middle section corresponds to the sandstone reservoir. (b) Histogram of the permeability field for the reservoir section.

$$M_{\text{VRH}} = \frac{M_{\text{Voigt}} + M_{\text{Reuss}}}{2}, \quad (6)$$

where M_{Voigt} and M_{Reuss} are the Voigt upper and Reuss bound of the elastic modulus, respectively.

Then, we compute the bulk and shear modulus at critical porosity using the following equations (Dadashpour et al., 2008; Zhong et al., 2019b):

$$K_{\text{HM}} = \sqrt{\kappa \frac{c^2(1-\phi_c)^2 G_{\text{matrix}}^2}{18\pi^2(1-\nu)^2} P_{\text{eff}}}, \quad (7)$$

$$G_{\text{HM}} = \frac{5-4\nu}{5(2-\nu)} \sqrt{\kappa \frac{3c^2(1-\phi_c)^2 G_{\text{matrix}}^2}{2\pi^2(1-\nu)^2} P_{\text{eff}}}, \quad (8)$$

where G_{HM} and K_{HM} are the shear and bulk modulus at critical porosity, respectively, ν is the Poisson's ratio, κ is the coordination number, which is dependent on the reservoir type (five in our case), c is the average number of grain contact points (its value is nine), and P_{eff} is the effective pressure that is the difference between the lithostatic and hydrostatic pressure.

The dry rock modulus (K_{dry}) and shear modulus (G_{dry}) can be calculated using bulk and shear modulus at critical porosity (Dadashpour et al., 2008)

$$K_{\text{dry}} = \left(\frac{\frac{\phi}{\phi_b}}{K_{\text{HM}} + \frac{4G_{\text{HM}}}{3}} + \frac{1-\frac{\phi}{\phi_b}}{K_{\text{matrix}} + \frac{4G_{\text{HM}}}{3}} \right)^{-1} + \frac{4G_{\text{HM}}}{3}, \quad (9)$$

$$G_{\text{dry}} = \left(\frac{\frac{\phi}{\phi_b}}{G_{\text{HM}} + \frac{\eta G_{\text{HM}}}{6}} + \frac{1-\frac{\phi}{\phi_b}}{G_{\text{matrix}} + \frac{\eta G_{\text{HM}}}{6}} \right)^{-1} - \frac{\eta G_{\text{HM}}}{6}, \quad (10)$$

where G_{HM} and K_{HM} are the bulk and shear modulus at critical porosity, respectively (Dadashpour et al., 2008), $\eta = (9K_{\text{HM}} + 8G_{\text{HM}})/(K_{\text{HM}} + 2G_{\text{HM}})$, and ϕ_b is the porosity at which the contact cement trend turns into a constant trend. The moduli are calculated from the contact cementation theory with $\phi_b = \phi$. Using the Gassmann fluid substitution theory (Gassmann,

1951), the bulk modulus (K_{sat}) and shear modulus (G_{sat}) can be calculated from the dry rock moduli and solid phase moduli (Mavko et al., 1998):

$$G_{\text{sat}} = G_{\text{dry}}, \quad (11)$$

$$K_{\text{sat}} = K_{\text{dry}} + \frac{1 - \frac{K_{\text{dry}}}{K_{\text{matrix}}}}{\frac{\phi}{K_f} + \frac{1-\phi}{K_{\text{matrix}}} - \frac{K_{\text{dry}}}{K_{\text{matrix}}}}. \quad (12)$$

After calculating the density, bulk modulus, and the shear modulus, P-wave velocity can be calculated as follows:

$$V_P = \sqrt{\left(K_{\text{sat}} + \frac{4G_{\text{sat}}}{3} \right) / \rho_b}. \quad (13)$$

To estimate the S-wave velocity (V_S), we use the empirical relationship between the P- and the S-wave velocities. For the shale facies, we use the mudrock line (Castagna and Backus, 1993), given by the following equation:

$$V_S = 0.862V_P - 1.172 \text{ (km/s)}. \quad (14)$$

For sand facies, we use the brine-saturated sandstone relationship (Castagna and Backus, 1993):

$$V_S = 0.804V_P - 0.856 \text{ (km/s)}. \quad (15)$$

We generate the time-lapse seismic response using the obtained velocity model using low-rank modeling and migration (Fomel et al., 2013). Equations 5 and 12 evince a nonlinear relationship between the rock properties and the fluid saturation S_a . The problem is nonlinear and a highly ill-posed inverse problem with high uncertainty. Therefore, a reasonable approach to this problem-solution space necessitates the use of deep learning, which helps to perform reservoir assessment under geologic uncertainty.

Network architecture and training

Generative adversarial networks (GANs) are a type of generative model that draw samples from a given distribution and learn to represent an estimate of that distribution (Goodfellow, 2016). GANs allow the representation of high-dimensional probability distributions, which are important for practical applications. GAN architecture consists of two networks that are simultaneously trained, that is, the generator (G) and the discriminator (D). The term G captures the data distribution and tries to mislead D by making D believe that the generated data are the real data. However, D behaves as a classifier that discriminates between the generated data and the real data and outputs the probability between zero and one depending upon how close the generated data are to the real data. During the training

Table 1. List of density, elastic properties, and fractions of rock minerals used in this study (Mavko et al., 1998).

Mineral	Fractions	Density (g/cm ³)	K (GPa)	G (GPa)
Clay	0.05	2.5	21	9
Quartz	0.65	2.65	36.6	44
Feldspar	0.2	2.63	75.6	25.6
Rock fragments	0.1	2.7	80	20

process, both networks optimize themselves, and the optimization process eventually tries to reach a Nash equilibrium, which is a stable system state that involves interaction between the two networks (Salehi et al., 2020).

GANs have computational as well as statistical advantages over other architectures. Some of its major computational advantages are that it can incorporate a wide variety of functions into the model and does not need Markov chains. GANs are designed to avoid using Markov chains because Markov chains while being a powerful tool for performing Bayesian inversion can be computationally prohibitive in high-dimensional spaces because they have slower convergence than single step generation methods (Goodfellow, 2016). Another advantage is that methods that are based on Markov chains require a blurry distribution for the chains to be able to mix between modes, whereas GANs can represent very sharp distributions. The major statistical advantage is that the generator network learns from the gradients flowing through the discriminator without the components of the input being copied directly into the generator's parameters (Goodfellow et al., 2014). GANs are designed to work with multimodal outputs, which is advantageous when a single input corresponds to multiple acceptable answers. This is an advantage over the conventional machine-learning algorithms that minimize mean-square error between the predicted and the desired output without producing multiple correct answers (Goodfellow, 2016).

To improve the approximation, the network needs to know the error between the prediction and the ground truth, which is known as the loss function. The loss function is extremely important in constraining the network and improving the approximations. Lotter et al. (2016) demonstrate that in case of multimodal outputs, the conventional neural networks are unable to produce sharp representations. When the predicted output has multiple correct answers, the conventional networks that use $L1$ or $L2$ norm in the loss function average out all the possibilities and produce a blurry output. Instead of averaging, the GAN framework puts the G against an adversary D , thus replacing the explicit loss function with another neural network. The gradients that accumulate from the loss function of D are used to update the G network. GANs are structured probabilistic models in which the cost function of both the players is defined in terms of their tuning parameters. The original loss function for GANs was designed as a minimax loss that simultaneously optimized the discriminator and generator models. In the minimax game, the generator loss is minimized, and the discriminator loss is maximized. The GAN framework needs to be well constrained to achieve convergence. In the current work, we adopt the framework shown in Figure 2.

The term G consists of three components: the encoder, the transformation layer, and the decoder as shown in Figure 3a.

The encoder is essentially a convolutional neural network that has filters to extract different input features. We use three convolution layers in the encoder with 32 filters in the initial layer. Each layer in the encoder progressively extracts higher level features. The transformation blocks map the feature vectors from the source domain to the target domain. We used six residual network (ResNet) blocks in which each block has two convolution layers. In each block, the residue of the input is added to the output such that the characteristics of the input image, such as the shape and size of the object, are retained in the output. In the decoder block, we build low-level features back from the feature vector by applying transpose convolution. The discriminator as shown in Figure 3b consists of five convolution layers with the last layer producing the probability of the output being real or fake. We use 64 filters in the initial layer of the discriminator.

We simultaneously train the generator and the discriminator network as shown in Figure 2. The network takes the input data (time-lapse seismic image) shown as input z and feeds it to generator 1 (G). This transforms the data from the source domain consisting of time-lapse seismic images to the target domain consisting of generated time-lapse CO_2 saturation change along with the plume extent. Then, the discriminator (D) discriminates between the generated change in CO_2 saturation and the original change in CO_2 saturation (shown as true label x). It outputs a value between zero and one that represents the likelihood of the sample being real. For a sample minibatch of m samples, the discriminator is updated by ascending the stochastic gradient given in equation 16. The discriminator loss in equation 16 consists of two terms corresponding to real and fake data. However, the generator is updated by descending the stochastic gradients (Goodfellow

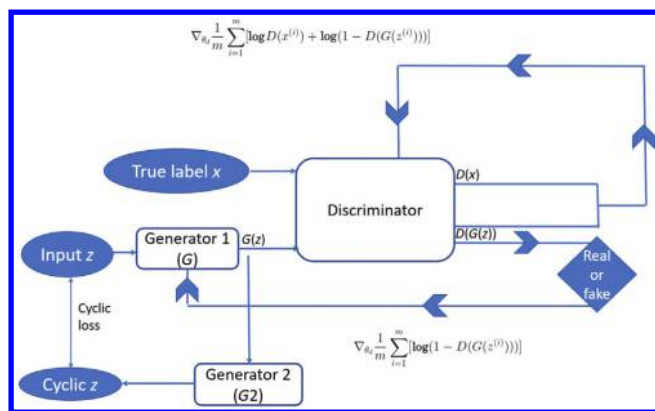


Figure 2. Implementation of the proposed algorithm: the generator (G) and the discriminator (D) are simultaneously trained to learn mapping from the input domain z consisting of time-lapse seismic images to the target domain x consisting of time-lapse CO_2 saturation change along with the plume extent. For a sample minibatch of m samples, the discriminator is updated by ascending the stochastic gradient, and the generator is updated by descending the stochastic gradients as shown by their respective equations.

et al., 2014) given in equation 17. The training procedure for the generator is such that it maximizes the probability of the discriminator making a mistake (Goodfellow et al., 2014). Goodfellow et al. (2014) show that maximizing the objective function of the discriminator (also known as nonsaturating GAN) works better in application compared with direct minimization of the discriminator objective function (also known as saturating GAN). In practice, the loss function shown in equation 17 may not provide sufficient gradient for training G . This happens in initial training stages when G is not well trained. The generated samples are different from the real samples, and D can reject samples with high confidence. This leads to the saturation of the $\log(1 - D(G(z)))$ term.

To improve the gradients, Goodfellow (2016) proposes training the generator to maximize $\log D(G(z))$ instead of minimizing $\log(1 - D(G(z)))$, thereby replacing equation 17 with equation 18

$$\text{grad}_D = \nabla_{\theta_d} \frac{1}{m} \sum_{i=1}^m [\log D(x^{(i)}) + \log(1 - D(G(z^{(i)})))] \quad (16)$$

$$\text{grad}_G = \nabla_{\theta_g} \frac{1}{m} \sum_{i=1}^m [\log(1 - D(G(z^{(i)})))] \quad (17)$$

$$\text{grad}_G = \nabla_{\theta_g} \frac{1}{m} \sum_{i=1}^m [-\log(D(G(z^{(i)})))] \quad (18)$$

Given the space of possible mapping functions, the aforementioned mapping alone cannot ensure the mapping of each instance of the input domain consisting of time-lapse seismic data to the target domain consisting of saturation change. To reduce the space of possible mapping functions, the generated image is then fed into

generator 2 ($G2$), which has a similar architecture to G (Zhu et al., 2017). The term $G2$ converts it back to a time-lapse seismic image, and the loss function between the original input and the output of $G2$, known as cyclic loss, is minimized, thereby retaining the cyclic consistency. In addition to constraining the mapping space, cyclic loss also helps to guide the training process and can be viewed as a form of regularization. It prevents the generator from mode collapse, thereby stabilizing the training by preventing any unnecessary loss of information.

Instead of learning the mapping from seismic to fluid saturation, we learn the mapping between the time-lapse seismic response and the corresponding change in saturation (obtained by subtracting the initial response prior to injection from all the instances) to mitigate the uncertain initial values before injection. We train the network with the Adam optimizer using 200 epochs. We use 40 time-lapse seismic response data sets and corresponding saturation-change slices and test on 110 slices corresponding to different porosity and permeability instances that are not a part of training.

To stabilize the training process, we take into consideration the following factors:

- 1) Vanishing gradients: Although training a DNN, use of activation functions such as Sigmoid or Tanh lead to exponentially decreasing gradients during back propagation. We overcome this issue by using leaky rectified linear activation (LReLU) as an activation function.
- 2) Minibatch discrimination: Minibatch discrimination provides a way to handle the mode-collapse issue (Salimans et al., 2016), which is one of the main failure modes for GANs. Mode collapse happens when the generator over optimizes for a given discriminator and rotates through a given set of output types. The generator maps several input values to the same output, and this prevents the discriminator from learning to differentiate between the output of the generator network. In this situation, the algorithm fails to converge to a distribution with the correct

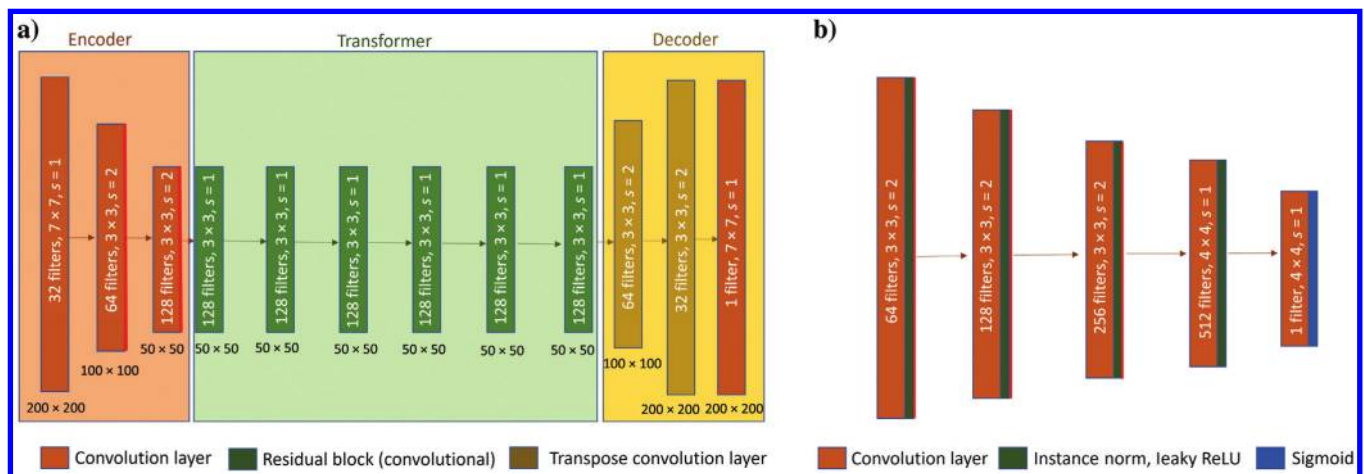


Figure 3. (a) Generator architecture and (b) discriminator architecture.

amount of entropy (Salimans et al., 2016). Using minibatch discrimination, the discriminator model looks at multiple examples in combination and therefore prevents the collapse of the generator. This eventually helps to improve training stability.

- 3) Replay buffer: One of the issues with adversarial training is that the discriminator network only focuses on recent refined images which can lead to drifting of the adversarial training. To improve the stability of training, we update the discriminator using a history of previously generated images so that the network retains the previous knowledge during incremental learning (Shrivastava et al., 2017).
- 4) Label smoothing: Label smoothing is a technique that aims to provide smoothed labels to the discriminator network. We smooth the target labels for the real as well as the fake images. It reduces the vulnerability of the model to adversarial examples (Salimans et al., 2016).
- 5) Instance normalization: We use instance normalization to normalize each feature map. This process allows the removal of instance-specific contrast information (Ulyanov et al., 2016) and, thus, simplifies the learning process of the model.

Geologic model

We demonstrate the proposed approach using a 2D vertical model that was used in Zhong et al. (2020). The model domain is discretized uniformly on a 128×128 grid as shown in Table 2. The 3200×32 m (denoted by X and Z in Table 2) model has a spatial sampling of 25 and 0.25 m (denoted by Δx and Δz in Table 2) in the horizontal and vertical directions, respectively. The reservoir model is divided into three different sections along the vertical direction. The upper (layers 1–10) and lower (layers 118–128) sections are shale layers and therefore serve as reservoir seals. The middle section corresponding to layers 11–118 is a sandstone formation that provides the storage reservoir for injected CO_2 . The reservoir top is at a depth of 1500 m from the surface, and at such depths, the injected CO_2 is assumed to be in a supercritical state. To model the phase behavior of the oil and gas phases, we use CMG GEM module that implements the Peng-Robinson equation (Peng and Robinson, 1976). For the storage section of the reservoir, we assume that the porosity and permeability are heterogeneous and generate them using

Table 2. Parameters used in the geologic model.

Dimensions	Value	Parameters	Value
$X \times Z$ (m)	3200×32	P_{ref} (MPa)	15
$\Delta x \times \Delta z$ (m)	25×0.25	Temp ($^{\circ}\text{C}$)	45
$N_x \times N_z$	128×128	CO_2	5×10^4
—	—	Injection rate	—

the sequential Gaussian simulation (SGSIM) algorithm from the open-source software package Stanford Geostatistical Modeling Software. We assume the permeability distribution to be ln normal with a mean (μ) of log (50 mD) and standard deviation σ of 0.5. However, this approach is not restricted to the multi-Gaussian distributions assumed in this work and can be applied to different methods that are used to generate the permeability. The porosity distribution is assumed to be linearly correlated with the log permeability and is calculated from the simulated permeability distribution using equation 1, with correlation lengths of 50 grid blocks (1250 m) in the x -direction and 10 grid blocks (2.5 m) in the z -direction. The shale layers in the upper and lower sections of the model are modeled as no-flow barriers by assigning low porosity ($\phi = 0.001$) and permeability ($k = 0.001$ mD) values to these layers. To create the training labels, we create a fluid model that consists of two components (CO_2 and brine) and two phases (liquid and gas), with fluid flux given in equation 2. We assume that the initial water saturation is 1 and irreducible water saturation is 0.20. We use CMG GEM (the module discretizes equations 2 and 3 into finite-difference forms) to simulate the water/gas saturation maps saved at monthly intervals as training and testing data sets corresponding to different porosity and permeability realizations. Initially, the top of the reservoir is at a pressure of 15 MPa and a constant temperature of 45°C . An injector with a total injection period of five years is located at the center of the reservoir (grid block 64, 64) with an injection rate fixed at 5×10^4 m³/day that is constrained by the maximum bottom hole pressure of 30 MPa. Then, using equations 5–14, we create the rock-physics model to find the relationship between the rock elastic properties (e.g., impedance) and the reservoir properties (e.g., fluid saturation). Equations 5–12 indicate a nonlinear relationship between the rock properties and the fluid saturation S_a . Therefore, we create a nonlinear model using GANs to learn the mapping from the changes in the seismic amplitudes to the changes in the saturation. We train the network using 40 different instances consisting of 4 time-lapse seismic data sets from 10 different porosity and permeability instances. The change in seismic response from prior to injection of the CO_2 to 1530 days after the CO_2 injection is shown in Figure 4. Figure 5a

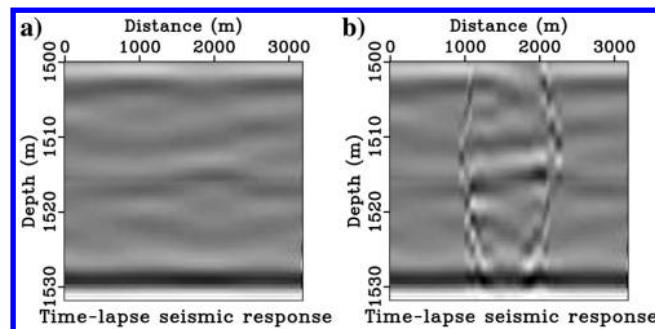


Figure 4. Seismic response change for one of the instances: (a) prior to injection and (b) 1530 days after CO_2 injection.

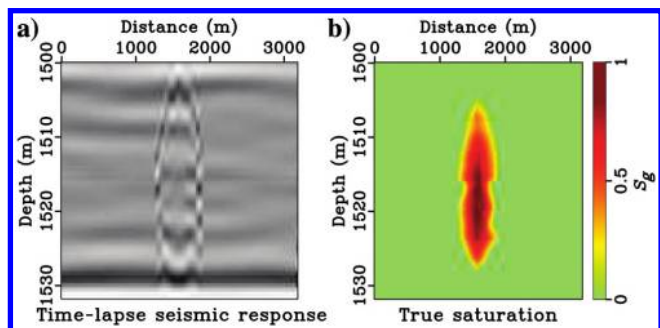


Figure 5. One of the training slices at time = 180 days. (a) Time-lapse seismic response and (b) change in saturation.

Figure 6. Slices at time = 180, 630, and 930 days, respectively. (a, d, and g) Time-lapse seismic response, (b, e, and h) predicted saturation change using the proposed method, and (c, f, and i) CMG simulation-based CO_2 saturation change (ΔS_g).

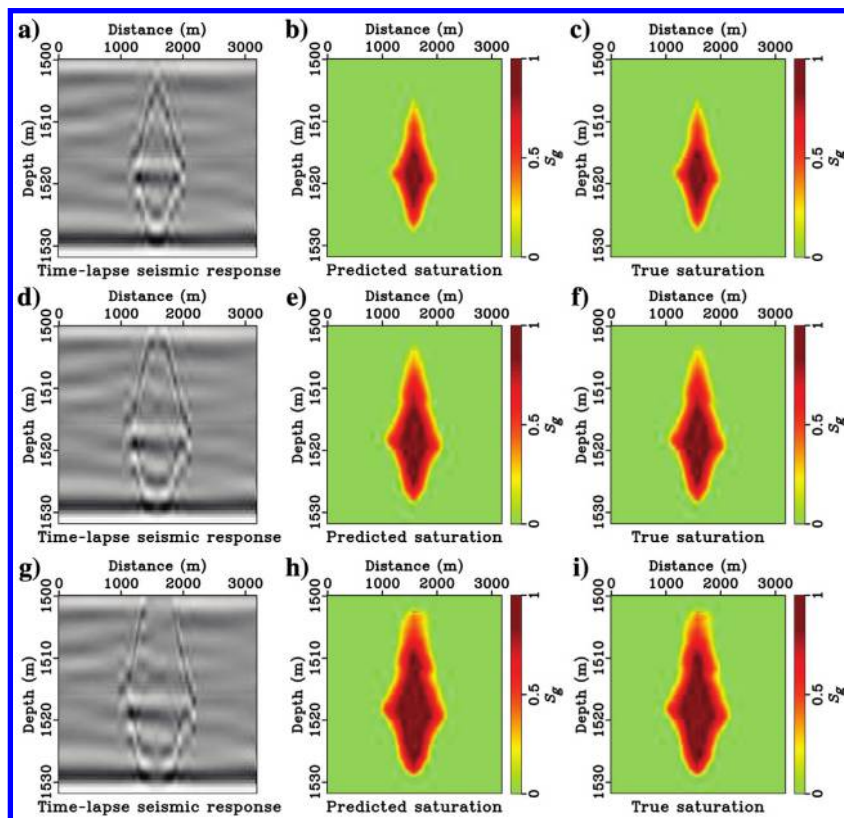
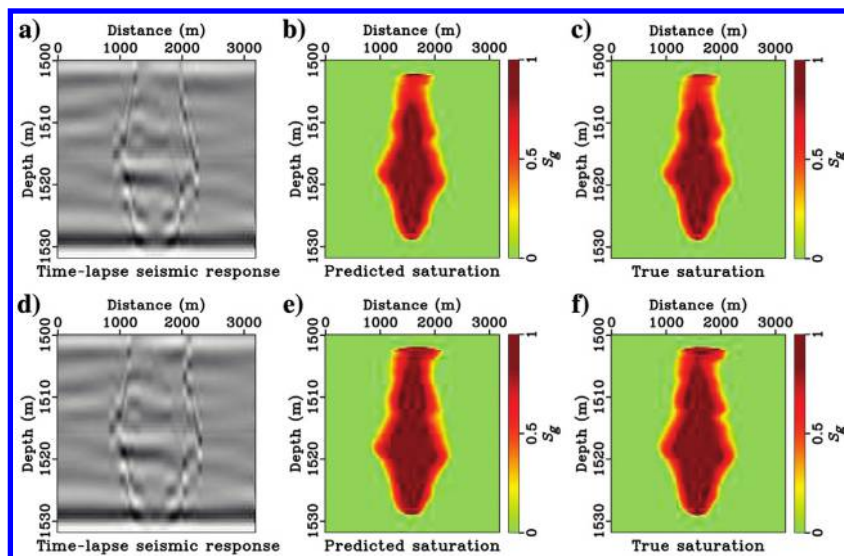


Figure 7. Slices at time = 1230 and 1530 days, respectively. (a and d) Time-lapse seismic response, (b and e) predicted saturation change using the proposed method, and (c and f) CMG simulation-based CO_2 saturation change (ΔS_g).



and 5b shows one of the training time slices. Once the network learns this mapping, we apply the learned weights on the test data set, which is not a part of the training. Figures 6a, 6d, 6g, 7a, 7d, 8a, 8d, 8g, 9a, and 9d show the test slices corresponding to different porosity and permeability values after 180, 630, 930, 1230, and 1530 days of CO_2 injection. We input these test slices into the pretrained network, and the network applies the weights learned during the training phase and outputs the change in saturation as shown in Figures 6b, 6e, 6h, 7b, 7e, 8b, 8e, 8h, 9b, and 9e. This is close to the true saturation as shown in Figures 6c, 6f, 6i, 7c, 7f, 8c, 8f, 8i, 9c, and 9f.

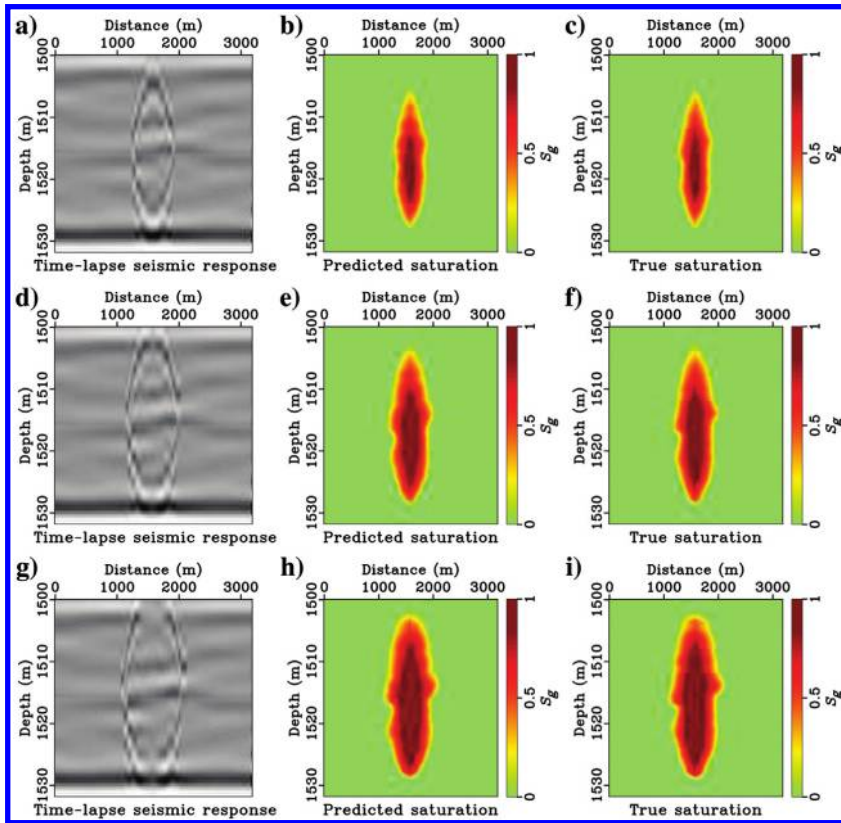


Figure 8. Slices from a different simulation at time = 180, 630, and 930 days, respectively. (a, d, and g) Time-lapse seismic response, (b, e, and h) predicted saturation change using the proposed method, and (c, f, and i) CMG simulation-based CO_2 saturation change (ΔS_g).

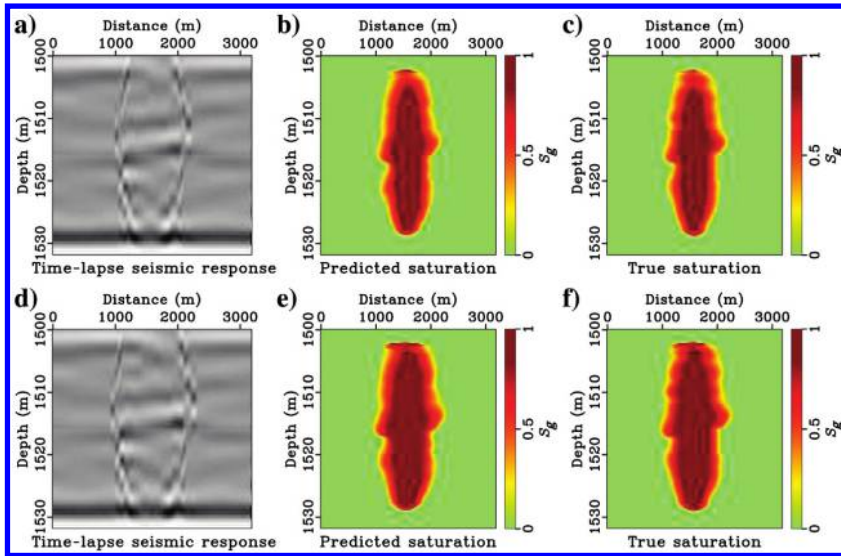


Figure 9. Slices from a different simulation at time = 1230 and 1530 days, respectively. (a and d) Time-lapse seismic response, (b and e) predicted saturation change using the proposed method, and (c and f) CMG simulation-based CO_2 saturation change (ΔS_g).

Performance metric

To quantify the performance of the proposed method, we use two different metrics: the structural similarity index (SSIM) (Wang et al., 2004) and the coefficient of determination (R^2). The SSIM is the measure of the “perpetual difference between two images.” Given the ground truth as x and prediction as y , it is defined as

$$\text{SSIM} = [l(x, y)]^\alpha \cdot [c(x, y)]^\beta \cdot [s(x, y)]^\gamma, \quad (19)$$

where $\alpha > 0, \beta > 0, \gamma > 0$ are the parameters used to adjust the relative importance of the three parameters that are luminance (l), contrast comparison function (c), and structure comparison function (s). The expression for SSIM is as follows:

$$\text{SSIM} = \frac{(2\mu_x\mu_y + C_1)(2\sigma_{xy} + C_2)}{(\mu_x^2 + \mu_y^2 + C_1)(\sigma_x^2 + \sigma_y^2 + C_2)}, \quad (20)$$

where μ_x and μ_y are the mean values for x and y , respectively, σ_x and σ_y are the standard deviations, σ_{xy} is the

covariance, and constant $C_1 = (K_1 L)^2$ and $C_2 = (K_2 L)^2$ is included to make the computation stable when $\mu_x^2 + \mu_y^2$ is close to zero. The term L is the dynamic range of the pixel values, and $K_1 < 1$, $K_2 < 1$ are small constants. For assessing the image quality, SSIM should be applied locally using sliding windows rather than globally. This is true for several reasons. First, the statistical features of the seismic data are highly spatially nonstationary;

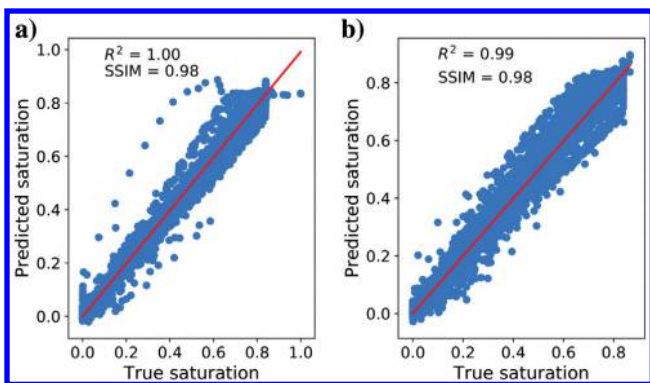


Figure 10. Plot of CO₂ saturation generated by the numerical simulations and saturation generated by the proposed method with R^2 and SSIM values (a) for the instance shown in Figure 7 and (b) for the instance shown in Figure 9.

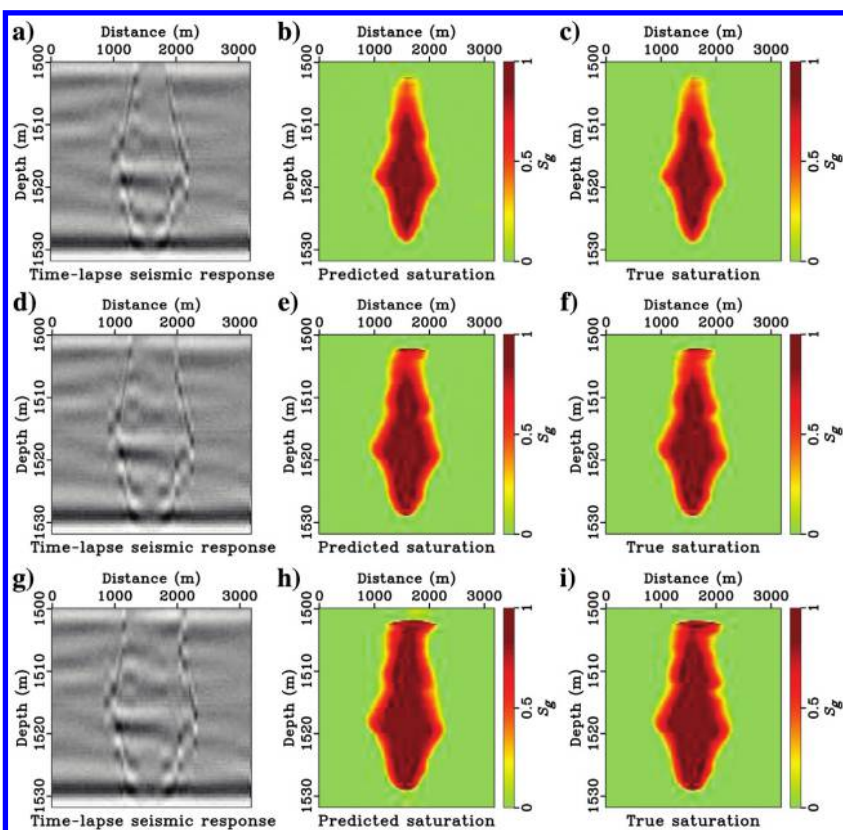


Figure 11. Test with noise. Slices at time = 930, 1230, and 1530 days, respectively. (a, d, and g) Time-lapse seismic response with noise, (b, e, and h) predicted saturation change using the proposed method, and (c, f, and i) CMG simulation-based CO₂ saturation change (ΔS_g).

second, the distortion or the noise, which may or may not depend on the statistical features of the data, also can be spatially variant; and finally, the localized measurement provides a spatially variant quality map of the data that in turn provides detailed information about the quality degradation of the data (Wang et al., 2004).

The second metric that we use is the coefficient of determination (R^2). The term R^2 is a statistical measure of the closeness between two variables and is defined as

$$R^2 = 1 - \frac{\sum_{i=1}^N (y^i - \hat{y}^i)^2}{\sum_{i=1}^N (y^i - \bar{y})^2}, \quad (21)$$

where y^i and \hat{y}^i are the original samples and the generated samples using the proposed algorithm, respectively, \bar{y} is the mean of the original samples, and N is the number of samples.

Figure 10a and 10b shows the high SSIM and R^2 values for both the test slices, which indicates that the output of the proposed method is close to the true saturation values.

Robustness of the proposed method to noise

With the rapid development of deep-learning techniques, it is important to ensure the robustness of the designed models. Recent research has revealed that the deep-learning models are vulnerable to adversarial attacks. Although the fabricated samples can be perceived as normal by the human eye, the deep-learning models start giving incorrect predictions with the fabricated models. Therefore, for practical applications, it is important to design networks keeping in mind the adversarial attacks and defense mechanisms (Ren et al., 2020). Adversarial training serves as a defense against adversarial samples and improves the robustness of the network during training. This property of GANs helps to mitigate the adversarial attacks that are the perturbations imperceptible to human vision but sufficient for the model to make an incorrect prediction (Ren et al., 2020). To test the robustness of the proposed method to noise, we add white noise to the input seismic data during the test phase. Figures 11a, 11d, 11g, 12a, 12d, and 12g show input seismic data with added noise for two different data sets. Figures 11b, 11e, 11h, 12b, 12e, and 12h show the CO₂ saturation values along with the plume extent predicted by the network, which are close to the true saturation as shown in Figures 11c, 11f, 11i, 12c, 12f, and 12i.

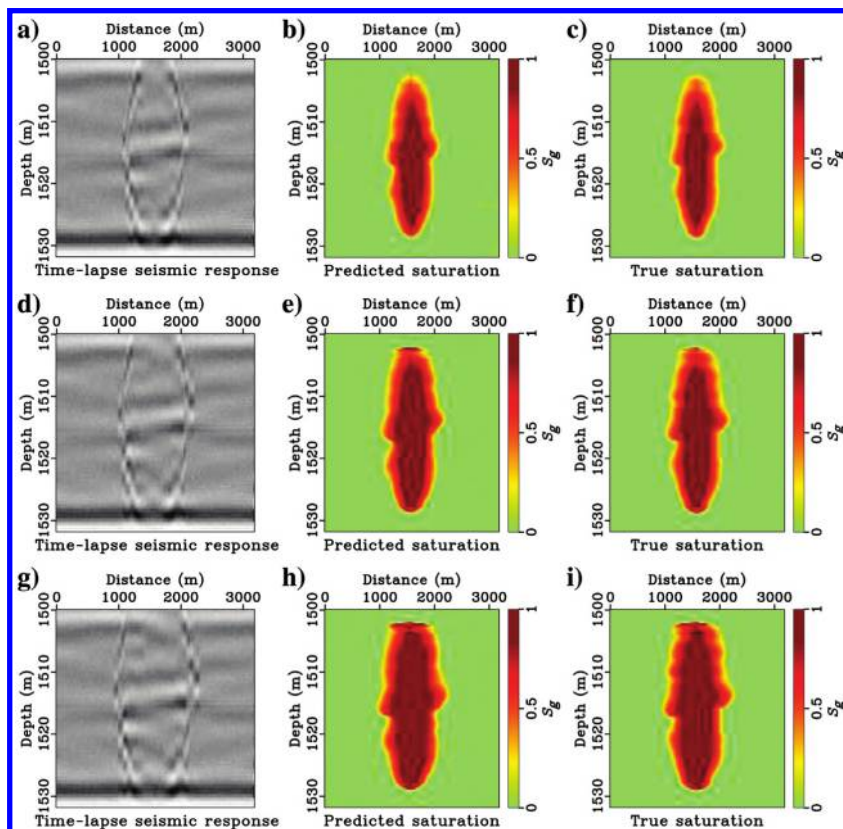


Figure 12. Test with noise. Slices from a different simulation at time = 930, 1230, and 1530 days, respectively. (a, d, and g) Time-lapse seismic response with noise, (b, e, and h) predicted saturation change using the proposed method, and (c, f, and i) CMG simulation-based CO₂ saturation change (ΔS_g).

Conclusion

We present a robust and effective framework for 4D seismic inversion for the estimation of dynamic reservoir properties like CO₂ saturation with plume tracking. The proposed method helps to perform rapid reservoir assessment for fluid-property (e.g., CO₂ saturation) changes that are highly accurate and efficient relative to the conventional methods. The proposed method incorporates geologic uncertainty by learning the data distribution through adversarial learning without requiring any explicit a priori information about the error distribution, which is usually difficult to ascertain. During the testing phase, the proposed method circumvents the intermediate steps consisting of iterative inversions involved in saturation computation from porosity and permeability distribution and, thus, is more efficient than the previously developed algorithms. The proposed workflow can be implemented on field data sets by training the network using simulations constrained by the acquisition geometry and frequency content of the field seismic data and the subsurface geology of the target reservoir.

Acknowledgments

We thank the sponsors of Gulf Coast Carbon Sequestration (GCCC) group and Texas Consortium of

Computational Seismology (TCCS) for their financial support. We also would like to thank Nvidia for providing us the Titan X GPU, which was used for running this algorithm. The computations in this paper were done using the Madagascar software package and Pytorch. A. Sun was partly supported by the Department of Energy National Energy Technology Laboratory (NETL) under grant DE-FE0031544.

Data and materials availability

Data associated with this research are available and can be obtained by contacting the corresponding author

References

- Assunção, G. S., A. Davolio, and D. J. Schiozer, 2016, A methodology to integrate multiple simulation models and 4D seismic data considering their uncertainties: Presented at the Annual Technical Conference and Exhibition, SPE.
- Bachrach, R., 2006, Joint estimation of porosity and saturation using stochastic rock-physics modeling: *Geophysics*, **71**, no. 5, O53–O63, doi: [10.1190/1.2235991](https://doi.org/10.1190/1.2235991).
- Batzle, M., and Z. Wang, 1992, Seismic properties of pore fluids: *Geophysics*, **57**, 1396–1408, doi: [10.1190/1.1443207](https://doi.org/10.1190/1.1443207).
- Buland, A., and Y. El Ouair, 2006, Bayesian time-lapse inversion: *Geophysics*, **71**, no. 3, R43–R48, doi: [10.1190/1.2196874](https://doi.org/10.1190/1.2196874).
- Castagna, J. P., and M. M. Backus, 1993, Offset-dependent reflectivity — Theory and practice of AVO analysis: SEG.
- Chadwick, R. A., B. P. Marchant, and G. A. Williams, 2014, CO₂ storage monitoring: Leakage detection and measurement in subsurface volumes from 3D seismic data at Sleipner: *Energy Procedia*, **63**, 4224–4239, doi: [10.1016/j.egypro.2014.11.458](https://doi.org/10.1016/j.egypro.2014.11.458).
- Dadashpour, M., M. Landrø, and J. Kleppe, 2008, Nonlinear inversion for estimating reservoir parameters from time-lapse seismic data: *Journal of Geophysics and Engineering*, **5**, 54–66, doi: [10.1088/1742-2132/5/1/006](https://doi.org/10.1088/1742-2132/5/1/006).
- Dai, Z., H. Viswanathan, J. Fessenden-Rahn, R. Middleton, F. Pan, W. Jia, S.-Y. Lee, B. McPherson, W. Ampomah, and R. Grigg, 2014, Uncertainty quantification for CO₂ sequestration and enhanced oil recovery: *Energy Procedia*, **63**, 7685–7693, doi: [10.1016/j.egypro.2014.11.802](https://doi.org/10.1016/j.egypro.2014.11.802).
- Eidsvik, J., P. Avseth, H. Omre, T. Mukerji, and G. Mavko, 2004, Stochastic reservoir characterization using pre-stack seismic data: *Geophysics*, **69**, 978–993, doi: [10.1190/1.1778241](https://doi.org/10.1190/1.1778241).

- Eiken, O., 2019, Twenty years of monitoring CO₂ injection at Sleipner, in T. L. Davis, M. Landro, and M. Wilson, eds., *Geophysics and geosequestration*: Cambridge University Press, 209–234.
- Fomel, S., L. Ying, and X. Song, 2013, Seismic wave extrapolation using lowrank symbol approximation: *Geophysical Prospecting*, **61**, 526–536, doi: [10.1111/j.1365-2478.2012.01064.x](https://doi.org/10.1111/j.1365-2478.2012.01064.x).
- Fu, H., Y. Zhang, and M. Ma, 2019, Seismic waveform inversion using a neural network-based forward: *Journal of Physics: Conference Series*, **1324**, 012043, doi: [10.1088/1742-6596/1324/1/012043](https://doi.org/10.1088/1742-6596/1324/1/012043).
- Gassmann, F., 1951, Elastic waves through a packing of spheres: *Geophysics*, **16**, 673–685, doi: [10.1190/1.1437718](https://doi.org/10.1190/1.1437718).
- Gibson-Poole, C., and S. Raikes, 2010, Enhanced understanding of CO₂ storage at Krechba from 3D seismic: *Proceedings of the 9th Annual Conference on Carbon Capture and Sequestration*, 10–13.
- Goodfellow, I., 2016, NIPS 2016 tutorial: Generative adversarial networks: arXiv preprint, arXiv:1701.00160.
- Goodfellow, I., J. Pouget-Abadie, M. Mirza, B. Xu, D. Warde-Farley, S. Ozair, A. Courville, and Y. Bengio, 2014, Generative adversarial nets: *Advances in Neural Information Processing Systems*, 2672–2680.
- Grana, D., and E. Della Rossa, 2010, Probabilistic petrophysical-properties estimation integrating statistical rock physics with seismic inversion: *Geophysics*, **75**, no. 3, O21–O37, doi: [10.1190/1.3386676](https://doi.org/10.1190/1.3386676).
- Grana, D., and T. Mukerji, 2015, Bayesian inversion of time-lapse seismic data for the estimation of static reservoir properties and dynamic property changes: *Geophysical Prospecting*, **63**, 637–655, doi: [10.1111/1365-2478.12203](https://doi.org/10.1111/1365-2478.12203).
- Ivanova, A., A. Kashubin, N. Juhojuntti, J. Kummerow, J. Henningsen, C. Juhlin, S. Lüth, and M. Ivandic, 2012, Monitoring and volumetric estimation of injected CO₂ using 4D seismic, petrophysical data, core measurements and well logging: A case study at Ketzin, Germany: *Geophysical Prospecting*, **60**, 957–973, doi: [10.1111/j.1365-2478.2012.01045.x](https://doi.org/10.1111/j.1365-2478.2012.01045.x).
- Johansen, T. A., E. H. Jensen, G. Mavko, and J. Dvorkin, 2013, Inverse rock physics modeling for reservoir quality prediction: *Geophysics*, **78**, no. 2, M1–M18, doi: [10.1190/geo2012-0215.1](https://doi.org/10.1190/geo2012-0215.1).
- Johansen, T. A., K. Spikes, and J. Dvorkin, 2004, Strategy for estimation of lithology and reservoir properties from seismic velocities and density: 74th Annual International Meeting, SEG, Expanded Abstracts, 1726–1729, doi: [10.1190/1.1845162](https://doi.org/10.1190/1.1845162).
- Kazemeini, S. H., C. Juhlin, and S. Fomel, 2010, Monitoring CO₂ response on surface seismic data; a rock physics and seismic modeling feasibility study at the CO₂ sequestration site, Ketzin, Germany: *Journal of Applied Geophysics*, **71**, 109–124, doi: [10.1016/j.jappgeo.2010.05.004](https://doi.org/10.1016/j.jappgeo.2010.05.004).
- Landrø, M., 2001, Discrimination between pressure and fluid saturation changes from time-lapse seismic data: *Geophysics*, **66**, 836–844, doi: [10.1190/1.1444973](https://doi.org/10.1190/1.1444973).
- Landrø, M., H. H. Veire, K. Duffaut, and N. Najjar, 2003, Discrimination between pressure and fluid saturation changes from marine multicomponent time-lapse seismic data: *Geophysics*, **68**, 1592–1599, doi: [10.1190/1.1620633](https://doi.org/10.1190/1.1620633).
- Lotter, W., G. Kreiman, and D. Cox, 2016, Deep predictive coding networks for video prediction and unsupervised learning: arXiv preprint, arXiv:1605.08104.
- Lumley, D., 2010, 4D seismic monitoring of CO₂ sequestration: *The Leading Edge*, **29**, 150–155, doi: [10.1190/1.3304817](https://doi.org/10.1190/1.3304817).
- Maleki, M., A. Davolio, and D. J. Schiozer, 2018, Using simulation and production data to resolve ambiguity in interpreting 4D seismic inverted impedance in the Norne Field: *Petroleum Geoscience*, **24**, 335–347, doi: [10.1144/petgeo2017-032](https://doi.org/10.1144/petgeo2017-032).
- Mavko, G., T. Mukerji, and J. Dvorkin, 1998, *The rock physics handbook: Tools for seismic analysis in porous media*: University of Cambridge.
- Peng, D.-Y., and D. B. Robinson, 1976, A new two-constant equation of state: *Industrial & Engineering Chemistry Fundamentals*, **15**, 59–64, doi: [10.1021/i160057a011](https://doi.org/10.1021/i160057a011).
- Pevzner, R., M. Urosevic, D. Popik, V. Shulakova, K. Ter-tysnikov, E. Caspari, J. Correa, T. Dance, A. Kepic, S. Glubokovskikh, and S. Ziramov, 2017, 4D surface seismic tracks small supercritical CO₂ injection into the subsurface: CO₂CRC Otway Project: *International Journal of Greenhouse Gas Control*, **63**, 150–157, doi: [10.1016/j.ijggc.2017.05.008](https://doi.org/10.1016/j.ijggc.2017.05.008).
- Ren, K., T. Zheng, Z. Qin, and X. Liu, 2020, Adversarial attacks and defenses in deep learning: *Engineering*, **6**, 346–360, doi: [10.1016/j.eng.2019.12.012](https://doi.org/10.1016/j.eng.2019.12.012).
- Richardson, A., 2018, Seismic full-waveform inversion using deep learning tools and techniques: arXiv preprint, arXiv:1801.07232.
- Ringrose, P., A. Mathieson, I. Wright, F. Selama, O. Hansen, R. Bissell, N. Saoula, and J. Midgley, 2013, The In Salah CO₂ storage project: Lessons learned and knowledge transfer: *Energy Procedia*, **37**, 6226–6236, doi: [10.1016/j.egypro.2013.06.551](https://doi.org/10.1016/j.egypro.2013.06.551).
- Salehi, P., A. Chalechale, and M. Taghizadeh, 2020, Generative adversarial networks (GANs): An overview of theoretical model, evaluation metrics, and recent developments: arXiv preprint, arXiv:2005.13178.
- Salimans, T., I. Goodfellow, W. Zaremba, V. Cheung, A. Radford, and X. Chen, 2016, Improved techniques for training GANs: arXiv preprint, arXiv:1606.03498.
- Shrivastava, A., T. Pfister, O. Tuzel, J. Susskind, W. Wang, and R. Webb, 2017, Learning from simulated and unsupervised images through adversarial training: *Proceedings of the IEEE Conference on Computer Vision and Pattern Recognition*, 2107–2116.
- Sun, A. Y., M. Zeidouni, J.-P. Nicot, Z. Lu, and D. Zhang, 2013, Assessing leakage detectability at geologic CO₂ sequestration sites using the probabilistic collocation method: *Advances in Water Resources*, **56**, 49–60, doi: [10.1016/j.advwatres.2012.11.017](https://doi.org/10.1016/j.advwatres.2012.11.017).

- Sun, N.-Z., and A. Sun, 2015, Model calibration and parameter estimation: For environmental and water resource systems: Springer.
- Tarantola, A., 2005, Inverse problem theory and methods for model parameter estimation: SIAM.
- Tian, S., and C. MacBeth, 2015, An engineering-consistent Bayesian scheme for 4D seismic to simulator inversion: 77th EAGE Conference and Exhibition-Workshops, Extended Abstracts, 1–5, doi: [10.3997/2214-4609.201413159](https://doi.org/10.3997/2214-4609.201413159).
- Trani, M., R. Arts, O. Leeuwenburgh, and J. Brouwer, 2011, Estimation of changes in saturation and pressure from 4D seismic AVO and time-shift analysis: *Geophysics*, **76**, no. 2, C1–C17, doi: [10.1190/1.3549756](https://doi.org/10.1190/1.3549756).
- Ulyanov, D., A. Vedaldi, and V. Lempitsky, 2016, Instance normalization: The missing ingredient for fast stylization: arXiv preprint, arXiv:1607.08022.
- Vasco, D., M. Alfi, S. A. Hosseini, R. Zhang, T. Daley, J. B. Ajo-Franklin, and S. D. Hovorka, 2019, The seismic response to injected carbon dioxide: Comparing observations to estimates based upon fluid flow modeling: *Journal of Geophysical Research, Solid Earth*, **124**, 6880–6907, doi: [10.1029/2018JB016429](https://doi.org/10.1029/2018JB016429).
- Vasco, D. W., R. C. Bissell, B. Bohloli, T. M. Daley, A. Ferretti, W. Foxall, B. P. Goertz-Allmann, V. Korneev, J. P. Morris, V. Oye, and A. Ramirez, 2018, Monitoring and modeling caprock integrity at the In Salah carbon dioxide storage site, Algeria: *Geological Carbon Storage: Subsurface Seals and Caprock Integrity*, **238**, 243.
- Wang, Y., Q. Ge, W. Lu, and X. Yan, 2020, Well-logging constrained seismic inversion based on closed-loop convolutional neural network: *IEEE Transactions on Geoscience and Remote Sensing*, **58**, 5564–5574, doi: [10.1109/TGRS.2020.2967344](https://doi.org/10.1109/TGRS.2020.2967344).
- Wang, Z., A. C. Bovik, H. R. Sheikh, and E. P. Simoncelli, 2004, Image quality assessment: From error visibility to structural similarity: *IEEE Transactions on Image Processing*, **13**, 600–612, doi: [10.1109/TIP.2003.819861](https://doi.org/10.1109/TIP.2003.819861).
- White, D., 2011, Geophysical monitoring of the Weyburn CO₂ flood: Results during 10 years of injection: *Energy Procedia*, **4**, 3628–3635, doi: [10.1016/j.egypro.2011.02.293](https://doi.org/10.1016/j.egypro.2011.02.293).
- White, D. J., L. A. Roach, and B. Roberts, 2015, Time-lapse seismic performance of a sparse permanent array: Experience from the Aquistore CO₂ storage site-sparse permanent-array performance: *Geophysics*, **80**, no. 2, WA35–WA48, doi: [10.1190/geo2014-0239.1](https://doi.org/10.1190/geo2014-0239.1).
- Zhang, R., D. Vasco, T. M. Daley, and W. Harbert, 2015, Characterization of a fracture zone using seismic attributes at the In Salah CO₂ storage project: Interpretation, **3**, no. 2, SM37–SM46, doi: [10.1190/INT-2014-0141.1](https://doi.org/10.1190/INT-2014-0141.1).
- Zheng, Y., and Q. Zhang, 2018, Pre-stack seismic inversion with deep learning: First EAGE/PESGB Workshop Machine Learning, European Association of Geoscientists & Engineers, 1–4, doi: [10.3997/2214-4609.201803008](https://doi.org/10.3997/2214-4609.201803008).
- Zhong, Z., S. Liu, T. R. Carr, A. Takbiri-Borujeni, M. Kazemi, and Q. Fu, 2019a, Numerical simulation of water-alternating-gas process for optimizing EOR and carbon storage: *Energy Procedia*, **158**, 6079–6086, doi: [10.1016/j.egypro.2019.01.507](https://doi.org/10.1016/j.egypro.2019.01.507).
- Zhong, Z., A. Y. Sun, and H. Jeong, 2019b, Predicting CO₂ plume migration in heterogeneous formations using conditional deep convolutional generative adversarial network: *Water Resources Research*, **55**, 5830–5851, doi: [10.1029/2018WR024592](https://doi.org/10.1029/2018WR024592).
- Zhong, Z., A. Y. Sun, and X. Wu, 2020, Inversion of time-lapse seismic reservoir monitoring data using CycleGAN: A deep learning-based approach for estimating dynamic reservoir property changes: *Journal of Geophysical Research, Solid Earth*, **125**, e2019JB018408, doi: [10.1029/2019JB018408](https://doi.org/10.1029/2019JB018408).
- Zhu, J.-Y., T. Park, P. Isola, and A. A. Efros, 2017, Unpaired image-to-image translation using cycle-consistent adversarial networks: arXiv preprint, arXiv:1703.10593.

Biographies and photographs of the authors are not available.